Dynamics of linear polarization conversion in uniaxial crystals

Yana Izdebskaya[1,2], Etienne Brasselet[3], Vladlen Shvedov[1,2], Anton Desyatnikov[1], Wieslaw Krolikowski[1], and Yuri Kivshar[1]

[1]*Nonlinear Physics Centre and Laser Physics Centre, Research School of Physics and Engineering, The Australian National University, Canberra ACT 0200, Australia*
[2]*Department of Physics, Taurida National University, Simferopol 95007 Crimea, Ukraine*
[3]*Centre de Physique Moléculaire Optique et Hertzienne, Université Bordeaux 1, CNRS, 351 Cours de la Libération, 33405 Talence Cedex, France*

Abstract: We report on the experimental and theoretical investigation of polarization conversion of linearly polarized Gaussian beam propagating in perpendicularly cut homogeneous uniaxial crystals. We derive analytical expressions, in good agreement with experimental data, for power transfer between components at normal incidence accompanied by the generation of a topological quadrupole. We extend the results to the oblique incidence case and confirm experimentally the optimal parameters for generation of a single charge on-axis optical vortex, including spectrally resolved measurements for the white-light beams.

© 2009 Optical Society of America

OCIS codes: (260.1180) Crystal optics, (260.1440) Birefringence, (260.6042) Singular optics

References and links

1. J. F. Nye and M. V. Berry, "Dislocations in wave trains," Proc. R. Soc. London A **336**, 165 (1974).
2. M. S. Soskin and M. V. Vasnetsov, "Singular optics," Prog. Opt. **42**, 219 (Ed. E. Wolf, Elsevier, 2001).
3. M. R. Dennis, K. O'Holleran, and M. J. Padgett, "Singular Optics: Optical Vortices and Polarization Singularities," Prog. Opt. **52**, 293 (Ed. E. Wolf, Elsevier, 2009).
4. V. Bazhenov, M. Vasnetsov, and M. Soskin, "Laser beams with screw dislocations in their wavefonts," JETP Lett. **52**, 429 (1990).
5. N. Heckenberg, R. McDuff, C. Smith, and A. White, "Generation of optical phase singularities by computer-generated holograms," Opt. Lett. **17**, 221 (1992).
6. A. Ciattoni, G. Cincotti, and C. Palma, "Propagation of cylindrically symmetric fields in uniaxial crystals," J. Opt. Soc. Am. A **19**, 792 (2002).
7. A. Ciattoni, G. Cancotti, and C. Palma, "Circularly polarized beams and vortex generation in uniaxial media," J. Opt. Soc. Am. A **20**, 163 (2003).
8. A. Volyar and T. Fadeyeva, "Generation of singular beams in uniaxial crystals," Opt. Spectrosc. **94**, 235 (2003).
9. M. Berry and M. Dennis, "The optical singularities of birefringent dichroic chiral crystals," Proc. R. Soc. Lond. A **459**, 1261 (2003).
10. L. Marrucci, C. Manzo, and D. Paparo, "Optical spin-to-orbital angular momentum conversion in inhomogeneous anisotropic media," Phys. Rev. Lett. **96**, 163905 (2006).
11. E. Brasselet, N. Murazawa, H. Misawa, and S. Juodkazis, "Optical vortices from liquid crystal droplets," Phys. Rev. Lett. **103**, 103903 (2009).
12. A. V. Volyar and T. A. Fadeeva, "Optical vortices in crystals: Formation, annihilation, and decay of polarization ombilics," J. Techn. Phys. Lett. **29**, 111-114 (2003).
13. A. V. Volyar and T. A. Fadeeva, "Decay and fusion of polarization umbilics in a singular beam passed through a crystal," Opt. Spectrosc. **95**, 792-799 (2003).
14. Yu. Egorov, T. Fadeyeva, and A. Volyar, "The fine structure of singular beams in crystals: colours and polarization," J. Opt. A **6**, S217 (2004).
15. F. Flossmann, U. Schwarz, M. Maier, and M. Dennis, "Polarization singularities from unfolding an optical vortex through a birefringent crystal," Phys. Rev. Lett. **95**, 253901 (2005).

#116015 - $15.00 USD Received 20 Aug 2009; revised 18 Sep 2009; accepted 19 Sep 2009; published 24 Sep 2009

16. A. Volyar and T. Fadeyeva, "Laguerre-Gaussian beams with complex and real arguments in a uniaxial crystal," Opt. Spectrosc. **101**, 450-457 (2006).
17. T. Fadeyeva, Yu. Egorov, A. Rubass, G. A. Swartzlander, Jr., and A. Volyar, "Indistinguishability limit for off-axis vortex beams in uniaxial crystals," Opt. Lett. **32**, 3116 (2007).
18. T. Fadeyeva, A. Rubass, Yu. Egorov, A. Volyar, and G. Swartzlander, "Quadrefringence of optical vortices in a uniaxial crystal," J. Opt. Soc. Am. A **25**, 1634 (2008).
19. T. A. Fadeyeva, A. F. Rubass, and A. V. Volyar, "Transverse shift of a high-order paraxial vortex-beam induced by a homogeneous anisotropic medium," Phys. Rev. A **79**, 053815 (2009).
20. M. S. Soskin and M. V. Vasnetsov, "Nonlinear singular optics," Pure Appl. Opt. **7**, 301311 (1998).
21. A. S. Desyatnikov, Yu. S. Kivshar, and L. Torner, "Optical vortices and vortex solitons," Prog. Opt. **47**, 291-391 (Ed. E. Wolf, Elsevier, 2005).
22. D. N. Neshev, A. Dreischuh, V. Shvedov, A. S. Desyatnikov, W. Krolikowski, and Yu. S. Kivshar, "Observation of polychromatic vortex solitons," Opt. Lett. **33**, 1851 (2008).
23. V. G. Shvedov, A. S. Desyatnikov, A. V. Rode, W. Z. Krolikowski, and Yu. S. Kivshar, "Optical guiding of absorbing nanoclusters in air," Opt. Express **17**, 5743 (2009), http://www.opticsinfobase.org/oe/abstract.cfm?URI=oe-17-7-5743.
24. A. S. Desyatnikov, V. G. Shvedov, A. V. Rode, W. Z. Krolikowski, and Yu. S Kivshar, "Photophoretic manipulation of absorbing aerosol particles with vortex beams: theory versus experiment," Opt. Express, **17**, 8201 (2009), http://www.opticsinfobase.org/oe/abstract.cfm?URI=oe-17-10-8201.
25. E. Brasselet, Y. Izdebskaya, V. Shvedov, A. S. Desyatnikov, W. Krolikowski, and Yu. S. Kivshar, "Dynamics of optical spin-orbit coupling in uniaxial crystals," Opt. Lett. **34**, 1021-1023 (2009).
26. A. Volyar, V. Shvedov, T. Fadeyeva, A. S. Desyatnikov, D. N. Neshev, W. Krollikowski, and Yu. S. Kivshar, "Generation of single-charged optical vortices with a uniaxial crystal," Opt. Express **14**, 3724 (2006), http://www.opticsinfobase.org/oe/abstract.cfm?URI=oe-14-9-3724.
27. M. Berry, "Coloured phase singularities," New J. Phys. **4**, 66 (2002).
28. M. S. Soskin, P. V. Polyansky, and O. O. Arkheluyk, "Computer-synthesized hologram-based rainbow vortices," New J. Phys. **6**, 196 (2004).

1. Introduction

Circulating flows of electromagnetic energy, or optical vortices, appear in laser beams carrying phase singularities [1]. Fundamental properties and potential applications of optical vortices have attracted growing attention during last decade [2, 3]. A number of different techniques for generating optical vortices has been realized, among which the use of computer-generated holograms [4] and spiral phase plates [5] found the widest application. However, the capacity of anisotropic media to affect the polarization state of light can also be used to generate optical vortices in homogeneous [6–9] or inhomogeneous [10, 11] uniaxial crystals. In addition, phase singularities in scalar components, linearly or circularly polarized, are connected with polarization singularities of the total field [12–15] and their propagation dynamics and related topological reactions allow the observation of complex single- and multi-vortex beams [16–19].

Generation of optical vortices with uniaxial crystals has several advantages with respect to the most common strategies used in practical situations. Indeed the optical power limitation associated to computer-generated holograms, which is mainly due to inherent low diffraction efficiency of diffractive optical elements, is naturally overcome when using transparent birefringent crystals. On the other hand, the narrow spectral bandwidth constraint of spiral plates, which are basically designed for a well-defined wavelength, is intrinsically removed when dealing with the spin-to-orbital angular momentum coupling in anisotropic materials whose spectral dependence scales as the birefringence dispersion. In fact, both high optical power and spectrally broadband behavior are of importance when applications in nonlinear singular optics [20–22] and optical micro-manipulation [23, 24] are envisaged. However, while the efficiency of generation of the double-charge vortices can reach 50% using homogeneous uniaxial crystals over a broad spectral range [7, 25], the necessary conditions and limitations for generation of isolated single-charge vortex beams [26] remain unexplored.

In this paper we derive and analyze the solution of the paraxial wave equation for the on-axis and tilted linearly polarized fundamental Gaussian beams propagating in uniaxial crystals. We

#116015 - $15.00 USD Received 20 Aug 2009; revised 18 Sep 2009; accepted 19 Sep 2009; published 24 Sep 2009
(C) 2009 OSA

theoretically discuss the propagation dynamics and efficiency of polarization conversion in both cases and compare our predictions with experimental data. In particular, we derive the conditions for generation of the on-axis isolated single charge vortex in the case of oblique incidence and demonstrate that the generation efficiency can reach 75%. We also explore the influence of crystal chromatic dispersion on generation of white-light optical vortices, namely the relative shift of beams and rainbow coloring due to wavelength-dependent diffraction effects [26–28].

The paper is organized as follows. We first describe the general theoretical framework and the experimental setup in Sec. 2. Section 3 is then devoted to the normal incidence case and the generation of topological quadrupole. The single-charge isolated vortex beams are discussed in Sec. 4 and Sec. 5 summarizes the results.

2. Theoretical and experimental approaches

2.1. Paraxial solution

Let us consider the propagation of a light beam along the optical axis z of an uniaxial crystal, with transverse part of the complex envelope of the electric field of the form $\mathbf{E}(x,y,z)\exp(-i\omega t+ikn_o z)$, where ω is the frequency of light with time t, $k=2\pi/\lambda$ is the wavenumber in free space with the wavelength λ, and n_o is the ordinary refractive index of the crystal. Then, from Maxwell's equations, the well-known paraxial wave equation can be derived, assuming a slowly varying transverse envelope $\mathbf{E}$,

$$\left(\nabla_\perp^2+2ikn_o\partial_z\right)\mathbf{E}=\gamma\nabla_\perp\left(\nabla_\perp\cdot\mathbf{E}\right), \tag{1}$$

where $\nabla_\perp\equiv\mathbf{e}_x\partial_x+\mathbf{e}_y\partial_y$ and $\gamma=1-(n_o/n_e)^2$ with n_e the extraordinary refractive index of the crystal.

A modal solution, $\mathbf{E}(x,y,z)=\mathbf{c}_+E^+(u,v,z)+\mathbf{c}_-E^-(u,v,z)$, is conveniently obtained in the basis of circular polarizations, $\mathbf{c}_\pm=(\mathbf{e}_x\pm i\mathbf{e}_y)/\sqrt{2}$, and in terms of the variables $(u,v)=x\pm iy$. It reads $\mathbf{E}^{(s)}=(\mathbf{c}_+\partial_u\mp\mathbf{c}_-\partial_v)\Phi^{(s)}$, with the generating function satisfying $\left(i\beta_s\partial_z+\partial_{uv}^2\right)\Phi^{(s)}=0$, which naturally introduces the fundamental Gaussian solution $\Phi_0^{(s)}=G^{(s)}\equiv-(i\beta_s w^2/Z_s)\exp(i\beta_s uv/Z_s)$. Here $Z_s=z-i\beta_s w^2$ and w is the beam waist at the crystal input facet $z=0$. The signs $\mp$ in expression for $\mathbf{E}^{(s)}$ correspond, respectively, to the index $s\equiv o$ for the ordinary (TE) mode with $\beta_o=kn_o/2$, and $s\equiv e$ for the extraordinary (TM) mode with $\beta_e=kn_e^2/2n_o$.

Above formulation was directly used in Ref. [25] for the particular case of a circularly polarized incident Gaussian beam at the crystal input facet, namely $\mathbf{E}(r,z=0)=E_0\exp(-r^2/w^2)\,\mathbf{c}_\pm$ where $r=\sqrt{x^2+y^2}$. Here we extend this method for normally and obliquely incident linearly polarized Gaussian beams. The linearly polarized solutions are straightforwardly obtained from the circularly polarized by transformation of the basis, $\mathbf{e}_x=(\mathbf{c}_++\mathbf{c}_-)/\sqrt{2}$ and $\mathbf{e}_y=-i(\mathbf{c}_+-\mathbf{c}_-)/\sqrt{2}$. As an example, in the case of normal incidence, one obtains the following general solution for an incident linear polarization along x axis [6, 16, 18, 19], i.e. $\mathbf{E}(r,z=0)=E_0\exp(-r^2/w^2)\,\mathbf{e}_x$,

$$E_x = \frac{E_0}{2}\left\{G^{(e)}+G^{(o)}+\cos 2\varphi\left[G^{(e)}-G^{(o)}+\frac{i}{r^2}\left(\frac{Z_e}{\beta_e}G^{(e)}-\frac{Z_o}{\beta_o}G^{(o)}\right)\right]\right\}, \tag{2}$$

$$E_y = \frac{E_0}{2}\sin 2\varphi\left[G^{(e)}-G^{(o)}+\frac{i}{r^2}\left(\frac{Z_e}{\beta_e}G^{(e)}-\frac{Z_o}{\beta_o}G^{(o)}\right)\right], \tag{3}$$

where φ is the polar angle in cylindrical coordinates. More generally the input linearly polarized Gaussian has an arbitrary polarization plane defined by the angle φ_0, $\mathbf{E}(r,z=0)=E_0(\cos\varphi_0\,\mathbf{e}_x+\sin\varphi_0\,\mathbf{e}_y)\exp(-r^2/w^2)$, so that the solution above is given for $\varphi_0=0$. For the

#116015 - $15.00 USD Received 20 Aug 2009; revised 18 Sep 2009; accepted 19 Sep 2009; published 24 Sep 2009
(C) 2009 OSA

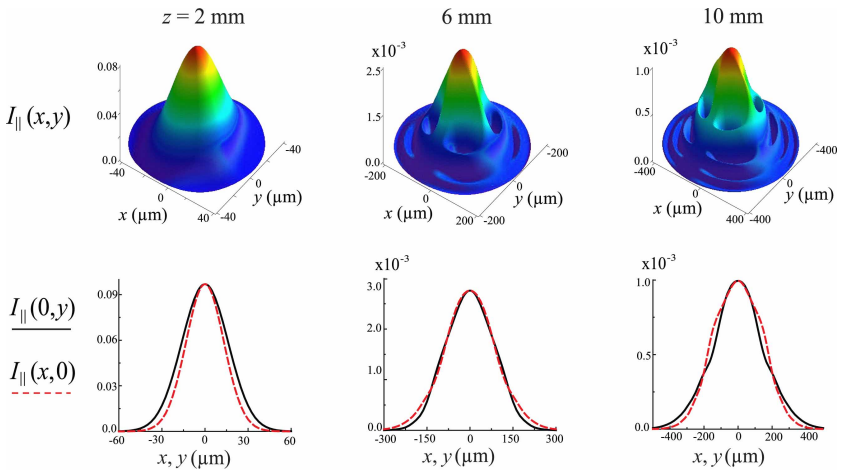

Fig. 1. Top row: intensity distributions $I_{\parallel} = |E_{\parallel}|^2$ of the field polarized parallel to the incident Gaussian beam ($\varphi_0 = 0$) with the waist $w = 4.6\,\mu$m in calcite crystal ($n_o = 1.656$ and $n_e = 1.485$ at $\lambda = 633$ nm). Bottom row: cross-sections along x (red dashed curves) and y (black solid curves).

y-polarized input beam, $\varphi_0 = \pi/2$, the solution is given by Eqs. (2, 3) with $E_x \leftrightarrow E_y$ and $\varphi \to \pi/2 - \varphi$. The general solution is obtained as a linear superposition and a convenient expression is written in terms of the linearly polarized components parallel and perpendicular to the polarization of the incident field, $E_{\parallel} = E_x \cos\varphi_0 + E_y \sin\varphi_0$ and $E_{\perp} = -E_x \sin\varphi_0 + E_y \cos\varphi_0$.

2.2. *The small birefringence limit*

Although the exact solution is explicitly known and is easy to compute numerically, a simple and useful representation can be derived in the limit of small birefringence. In fact, we note that uniaxial crystals have usually weak birefringence, $|n_o - n_e| \simeq 10^{-3} - 10^{-1}$, so that the anisotropy can be considered as a perturbation. Introducing the average refractive index $n = (n_o + n_e)/2$ and the small parameter $\varepsilon = (n_o - n_e)/n \ll 1$ we obtain $\beta_o \simeq \beta(1 + \varepsilon/2)$ and $\beta_e \simeq \beta(1 - 3\varepsilon/2)$, where $\beta = kn/2$. Expanding the expressions given by Eqs. (2, 3) with respect to ε and keeping only the terms of the leading order in ε we derive the following approximate representation for the general solution in the case of linearly polarized input Gaussian beam at normal incidence,

$$\begin{pmatrix} E_x \\ E_y \end{pmatrix} \simeq E_0 G \hat{\mathbf{M}} \begin{pmatrix} \cos\varphi_0 \\ \sin\varphi_0 \end{pmatrix}, \tag{4}$$

where $G = -(i\beta w^2/Z)\exp(i\beta r^2/Z)$ with $Z = z - iz_0$ and $z_0 = \beta w^2$. The electric field amplitude E_0 at $z = 0$ is related to the total input power $P_0 = \pi w^2 E_0^2/2$. The propagation matrix is given by

$$\hat{\mathbf{M}} = \begin{pmatrix} \cos\delta - i\sin\delta\cos 2\varphi & -i\sin\delta\sin 2\varphi \\ -i\sin\delta\sin 2\varphi & \cos\delta + i\sin\delta\cos 2\varphi \end{pmatrix}, \tag{5}$$

with complex $\delta = \varepsilon\beta r^2 z/Z^2$. Solution in this form is valid everywhere in the crystal if the anisotropy is small, $\varepsilon \ll 1$. Applying this limit below we will also use the following dimensionless coordinates: $\rho = r/w$ and $\zeta = z/z_0$, so that $\delta = \varepsilon\zeta\,[\rho/(\zeta - i)]^2$ and $G = (1 + i\zeta)^{-1}\exp[-\rho^2/(1 + i\zeta)]$.

#116015 - $15.00 USD Received 20 Aug 2009; revised 18 Sep 2009; accepted 19 Sep 2009; published 24 Sep 2009
(C) 2009 OSA

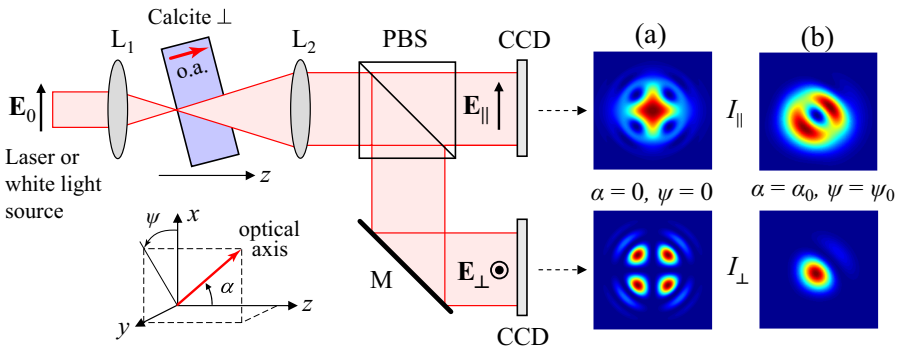

Fig. 2. Experimental setup. $L_{1,2}$: lenses or microobjectives; PBS: polarization beamsplitter; CCD: charge coupled device cameras; o.a.: optical axis, whose orientation is defined by the two angles α and ψ as shown in the inset. Intensities $I_{\parallel} = |\mathbf{E}_{\parallel}|^2$ and $I_{\perp} = |\mathbf{E}_{\perp}|^2$ for (a) normal and (b) oblique (see text for details) incidences, at the propagation length $z = 6$ mm for input beam waist $w = 4.6\,\mu$m in (a) and $w = 11\,\mu$m in (b); in both cases $\lambda = 633$ nm. Intensity distribution in panels (a,b) are false colored.

It is convenient in the following to operate with "parallel" and "perpendicular" components

$$\begin{pmatrix} E_{\parallel} \\ E_{\perp} \end{pmatrix} \simeq E_0 G \begin{pmatrix} \cos\delta - i\sin\delta\cos 2(\varphi-\varphi_0) \\ -i\sin\delta\sin 2(\varphi-\varphi_0) \end{pmatrix}, \tag{6}$$

in particular the parallel component acquires characteristic discrete set of zero intensity points – the topological quadrupole – see Fig. 1, top row. Note also that the usual transverse spreading associated with Gaussian beam divergence is anisotropic, in contrast to the case of isotropic media, which is due to different angular divergences of the ordinary and extraordinary waves [Fig. 1, bottom row].

2.3. *Experimental setup*

In our experiments we used uniaxial calcite crystal slabs that are cut perpendicularly to the optical axis into $10 \times 10 \times z$ mm^3 samples for $z = 1 \ldots 10$ mm with step of 1 mm, where the optical axis lies in the z direction. The setup is summarized in Fig. 2 and it is similar for both monochromatic or polychromatic light experiments, except for the preparation of the light beam. For the monochromatic case a linearly polarized light from He-Ne laser operating in the fundamental Gaussian mode at the wavelength $\lambda = 633$ nm is used whereas a quasi-Gaussian light beam is obtained from a halogen lamp with power 50 W and angular divergence 8° in experiments with white light. In the latter case, the polychromatic light from the lamp passes first through the bundle of optical fibers (with aperture 5 mm) and then through an infra-red filter which limits the spectral range to $440 - 800$ nm. The beam is collimated, after passing through a spatial filter, thereby attaining a nearly Gaussian intensity profile and polarization is made linear ($\mathbf{E}_0$) using a broadband birefringent polarizer. As shown in Fig. 2, the input beam (mono- or polychromatic) is focused onto the crystal by a first lens, or microobjective, L_1, and is further collimated by a second one L_2. The output beam passes through a polarizing beam-splitter (PBS) that separates the linearly polarized components parallel ($\mathbf{E}_{\parallel}$) and perpendicular ($\mathbf{E}_{\perp}$) to the incident beam polarization; their transverse intensity profiles are recorded on CCD video cameras.

The inset in Fig. 2 shows the geometry of crystal tilting, with ψ and α being the azimuthal and polar angles, respectively, that describe the optical axis orientation with respect to the

#116015 - $15.00 USD Received 20 Aug 2009; revised 18 Sep 2009; accepted 19 Sep 2009; published 24 Sep 2009
(C) 2009 OSA

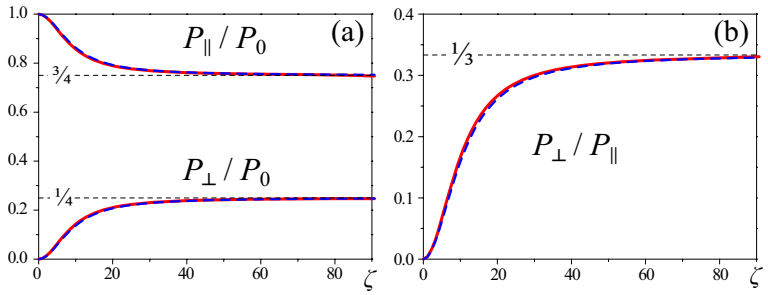

Fig. 3. Polarization conversion with respect to the normalized propagation distance in the case of normal incidence for $\lambda = 630$ nm and $\varepsilon = 0.109$. Solid red lines: numerical integration of exact solution (2, 3), and dashed blue lines: approximate formulas (7).

beam propagation direction. For normal incidence, i.e. $\alpha = 0$ and $\psi = 0$, the characteristic intensity patterns of coupled linearly polarized components are given by Eqs. (2, 3) and shown in Fig. 2(a). For a tilted crystal, there is a specific set of parameters $(\alpha_0(z), \psi_0(z))$, when at the distance z the beam acquires a on-axis single-charge vortex [26], with characteristic intensities in Fig. 2(b) obtained by direct integration of Eq. (1).

Finally, for polychromatic light the following dispersion law for ordinary and extraordinary refractive indices of calcite will be used in theoretical analysis, $n_o = (2.69705 + 0.0192064/(\lambda^2 - 0.01820) - 0.0151624\lambda^2)^{1/2}$ and $n_e = (2.18438 + 0.0087309/(\lambda^2 - 0.01018) - 0.0024411\lambda^2)^{1/2}$ where λ is expressed micrometers.

3. Normal incidence: topological quadrupole

3.1. *Efficiency of polarization conversion*

Experimentally accessible quantities to retrieve the propagation dynamics are the powers of orthogonally polarized field components at the output of a crystal with thickness z, $P_{\parallel,\perp}(z) = \iint |\, E_{\parallel,\perp}(x,y,z)\,|^2\, dxdy$. We use Eqs. (6) to explicitly calculate these powers in the limit of small birefringence $\varepsilon \ll 1$,

$$P_\parallel(\zeta) = P_0 - P_\perp(\zeta), \quad P_\perp(\zeta) = \frac{P_0}{4}\,\frac{\varepsilon^2\zeta^2(1+\zeta^2)^2}{\varepsilon^2\zeta^6 + (1+\zeta^2)^2}, \tag{7}$$

$$P_\perp(\zeta \ll 1) \simeq \frac{P_0}{4}\,\varepsilon^2\zeta^2, \quad P_\perp(\zeta \gg 1) \simeq \frac{P_0}{4}\,\frac{\varepsilon^2\zeta^2}{1+\varepsilon^2\zeta^2}, \tag{8}$$

in excellent agreement with exact numerical results, see Fig. 3, where P_0 is an input beam power.

Note that the parameters of the crystal (and their dispersion) enter these expressions through $\varepsilon(\lambda)$ while the use of normalized distance ζ allows to reveal the universal character of polarization conversion independently from the input beam waist w, see Fig. 3. It appears that the monotonous power conversion between linearly polarized components saturates at $P_\perp/P_\parallel \to 1/3$ as $\zeta \to \infty$. In contrast, for circular input polarization the output power ratio of circular orthogonally polarized components tends to unity [6, 25]. Obviously, there is no contradiction, which can be checked recalling that a linear polarization state may be described by the superposition of two coherent orthogonal circular polarization states with equal weights.

The experimental propagation dynamics of the polarization conversion for monochromatic light in the normal incidence case is presented in Fig. 4. The ratio $P_\perp/P_\parallel$ is measured as a function of z for $w = 1.8$ (black squares), 4.4 (red circles) and 11.2 μm (blue triangles) and

#116015 - $15.00 USD Received 20 Aug 2009; revised 18 Sep 2009; accepted 19 Sep 2009; published 24 Sep 2009
(C) 2009 OSA

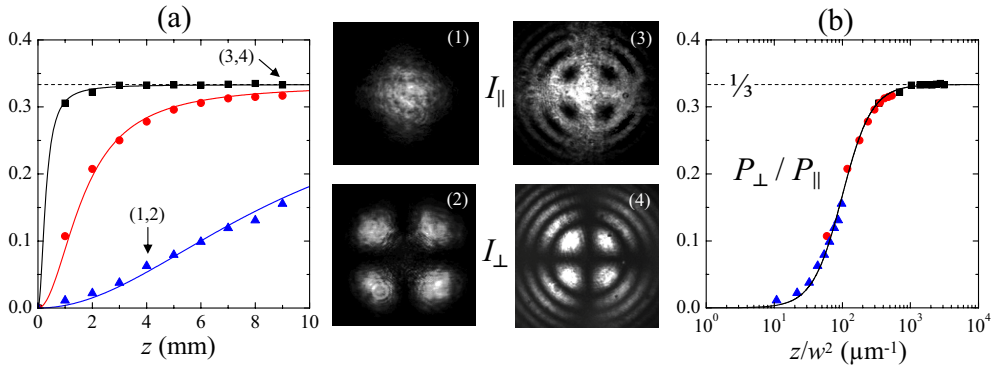

Fig. 4. (a) Ratio $P_\perp/P_\parallel$ as a function of the crystal thickness for three different waists for $\lambda = 0.6328\,\mu$m. Solid lines: theory; markers: experiment; black: $w = 1.8\,\mu$m; red: $w = 4.4\,\mu$m; blue: $w = 11.2\,\mu$m. (b) Power ratio $P_\perp/P_\parallel$ as a function of z/w^2 for the data of panel (a), the markers and the solid curve being respectively experimental data and theoretical prediction. The panels (1,2) correspond to the intensity distribution $I_{\parallel,\perp}$, respectively, and refer the set of parameters of the data indicated by the arrows in panel (a). Similarly, the panels (3,4) correspond to another set of parameters, see panel (a).

shown in Fig. 4(a). In all cases this ratio grows from zero to the expected asymptotic value $1/3$. While the multipole structure is not present for the lower power conversion efficiencies [see Fig. 4, panel (1)], larger conversion rate correspond to well-developed edges dislocations and multipole pattern for the perpendicular and parallel output ports, respectively [see Fig. 4, panels (3,4)]. We notice that the four panels shown in Fig. 4 can readily be compared visually since care was exercised to have identical maximal intensity values whatever are the values of crystal thickness and beam waist. These results are in good quantitative agreement with the predictions of the model that are represented as solid curves in Fig. 4(a).

The universal feature of polarization coupling unveiled in Fig. 3 is also confirmed experimentally, as demonstrated in Fig. 4(b) where $P_\perp/P_\parallel$ is plotted as a function of $z/w^2 = \beta\zeta$. Clearly, the rescaled data presented in Fig. 4(a) lies on the single calculated universal curve, which was recovered for waists values that almost (to a few percent) correspond to those experimentally extracted from asymptotic beam divergence measurements.

3.2. *Vortex trajectories*

It was shown recently that a single-charge on-axis optical vortex can be generated by tilting the incident linearly polarized beam with respect to the optical axis [26]. This is achieved by selecting one of the direction that corresponds to the single charge vortices location in the topological quadrupole at the crystal output facet. Below we explore in detail these locations for different parameters of the monochromatic beam as well as for polychromatic light.

The simplified analytical description of the problem in the limit of small birefringence [see Eqs. (6)] gives a convenient way to locate and characterize quantitatively the single charge optical vortices embedded in the field component whose polarization is parallel to the one of the incident beam, namely $E_\parallel = 0$. Introducing the real and imaginary parts, $\delta(\rho,\zeta) = A + iB$, we derive from Eqs. (6)

$$\cos A\,(\cosh B + \cos 2(\varphi - \varphi_0)\sinh B) = 0, \tag{9}$$

$$\sin A\,(\sinh B + \cos 2(\varphi - \varphi_0)\cosh B) = 0, \tag{10}$$

with $A = \varepsilon\rho^2\zeta(\zeta^2-1)/(1+\zeta^2)^2$ and $B = 2\varepsilon\rho^2\zeta^2/(1+\zeta^2)^2$. Since $B \geq 0$ we have $0 \leq$

#116015 - $15.00 USD Received 20 Aug 2009; revised 18 Sep 2009; accepted 19 Sep 2009; published 24 Sep 2009
(C) 2009 OSA

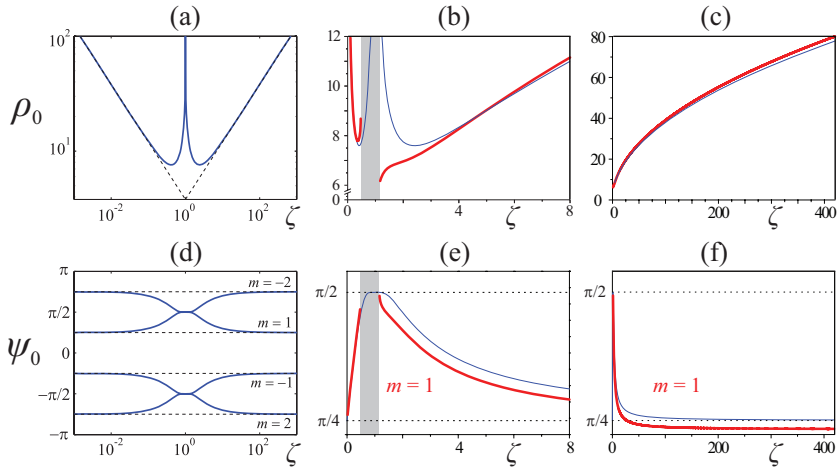

Fig. 5. Trajectories of single charge vortices which are the closest to the optical axis in reduced coordinates. (a-c) Distance from the optical axis ρ_0. (d-f) Polar angle ψ_0 in the (x,y) plane for $\varphi_0 = 0$. Blue curves: analytical expressions Eqs. (11, 12); dashed curves: asymptotes Eqs. (13, 14), and red curves: exact results Eqs. (2, 3).

$\tanh B < 1$ and it follows from Eq. (9) that $\cos A = 0$. Equation (10) thus gives $\cos 2(\varphi - \varphi_0) = -\tanh B$. We define the solutions to Eqs. (9, 10) as $\rho \equiv \rho_0(\zeta)$ and $\varphi \equiv \psi_0(\zeta)$, see Fig. 5. Restricting our considerations to the singularities that are the closest to the optical axis we obtain (in the interval $-\pi \le \varphi \le \pi$ and with $\varphi_0 = 0$)

$$\rho_0 = \sqrt{\frac{\pi}{2\varepsilon}}\,\frac{\zeta^2+1}{\sqrt{\zeta|\zeta^2-1|}}, \tag{11}$$

$$\psi_0 = \mathrm{sign}(m)\left\{(1-|m|)\,\pi + \frac{1}{2}\arccos\left[-\tanh\left(\frac{\pi\zeta}{|\zeta^2-1|}\right)\right]\right\}, \tag{12}$$

where $m = \pm 1, \pm 2$. Such trajectories are shown in Fig. 5(a, d) where the dashed lines correspond to asymptotic behavior for $\zeta \ll 1$ and $\zeta \gg 1$,

$$\rho_0 \simeq \sqrt{\frac{\pi}{2\varepsilon\zeta}} \quad \text{for} \quad \zeta \ll 1 \quad \text{and} \quad \rho_0 \simeq \sqrt{\frac{\pi\zeta}{2\varepsilon}} \quad \text{for} \quad \zeta \gg 1, \tag{13}$$

$$\psi_0 \simeq \left\{-\frac{3\pi}{4}, -\frac{\pi}{4}, \frac{\pi}{4}, \frac{3\pi}{4}\right\} \quad \text{for} \quad \zeta \ll 1 \quad \text{or} \quad \zeta \gg 1. \tag{14}$$

In addition, we determine the positions of field zeros using exact solution Eq. (2, 3). Corresponding radius ρ_0 (b, c) and the angle ψ_0 (e, f) are shown in Fig. 5 for short (b, e) and long (c, f) propagation distances (or crystal lengths). Note the differences with approximate solutions in (a, b): the exact asymptote $\rho_0 \simeq 3.907\sqrt{\zeta}$ is very close to $\sqrt{\pi\zeta/2\varepsilon} \simeq 3.798\sqrt{\zeta}$ and the exact limit $\psi_0(\zeta \to \infty) \to 0.235\pi$ in contrast to the approximate value 0.25π (for $m = 1$). Also noteworthy is that vortices disappear in a small region around $\zeta \sim 1$, as seen in shaded area in Fig. 5(b, e), through complex series of topological reactions; the details of this process can be easily reproduced by visualizing exact solution Eq. (2, 3).

The trajectories of individual single charge optical vortices embedded into the topological multipole in the case of normal incidence are retrieved by analyzing the intensity patterns $I_{\|}(x,y)$, see Fig. 2(a), as a function of the crystal thickness. From a practical point of view,

#116015 - $15.00 USD Received 20 Aug 2009; revised 18 Sep 2009; accepted 19 Sep 2009; published 24 Sep 2009
(C) 2009 OSA

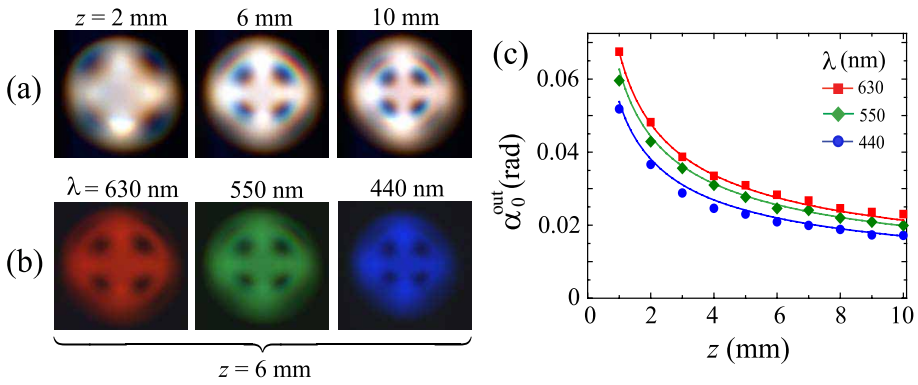

Fig. 6. (a) White light multipole at normal incidence for different propagation distance z inside the crystal (z =2, 6 and 10 mm). (b) Multipole spectral components, red (630 nm), green (550 nm) and blue (440 nm), for a crystal slab with fixed thickness 6 mm. (c) Angle defining the optical vortices trajectories as a function of the propagation distance for three different wavelengths; symbols: experimental data, solid curves: results from Eq. (15).

the minimal available thickness $z = 1$ mm leads us to investigate the asymptotic region $\zeta \gg 1$, see Eq. (13). The trajectory is conveniently described by the inclination angle of individual optical vortex with respect to the optical axis, $\tan\alpha_0 = r_0/z = \rho_0/(\zeta\beta w)$. In the small angle approximation, $\alpha_0 \ll 1$, it reduces to

$$\alpha_0 \simeq \sqrt{\frac{\lambda}{2z(n_o - n_e)}}. \tag{15}$$

Experimentally, the external (output) angle α_0^{out} is obtained by measuring the distances d_1 and d_2 between two diametrical vortices [see Fig. 6(a,b)] for two different positions, z_1 and z_2, of a screen placed at the output of the crystal after the lens L_2 has been removed (Fig. 2). Such a procedure gives $\tan\alpha_0^{\text{out}} = (d_2 - d_1)/2(z_2 - z_1)$. We found that α_0^{out} decreases with the propagation distance and increases with the wavelength. The corresponding results for three different wavelengths in the visible spectrum are summarized in Fig. 6(c) where the comparison using Eq. (15) is shown (solid curves) taking into account the refraction condition at the output interface, $\alpha_0^{\text{out}} = \sin^{-1}(n\sin\alpha_0)$. The agreement between theory and the experiment is excellent.

4. Oblique incidence: solitary vortices

4.1. *Vortex trajectories*

The model previously developed in the case of normal incidence can be extended to the tilted geometry where the optical axis now makes an angle α with the z axis in the meridional plane at an angle ψ from the (x,z) plane (see Fig. 2). For the purpose of demonstration we will consider a Gaussian beam linearly polarized along the x axis, i.e. $\varphi_0 = 0$. In order to benefit from the matrix formalism given by Eqs. (4, 5) it is convenient to introduce the cylindrical coordinates (r', φ, z') as illustrated in Fig. 7, which corresponds to the case $\psi = 0$.

Assuming $\alpha \ll 1$ and thereby neglecting the associated modifications of the matrix $\hat{\mathbf{M}}$, we simply need to account for the tilted nature of the reference Gaussian beam G in Eq. (4). From Fig. 7 we see that $\psi = 0$ and $\varphi = 0$ lead to $z' = \ell_1 + \ell_2$ with $\ell_1 = z\cos\alpha$ and $\ell_2 = r\sin\alpha$. The generalization to any (ψ, φ) is easily done by the transformation $\ell_2 \to \ell_2\cos(\varphi - \psi)$ and using

#116015 - $15.00 USD Received 20 Aug 2009; revised 18 Sep 2009; accepted 19 Sep 2009; published 24 Sep 2009
(C) 2009 OSA

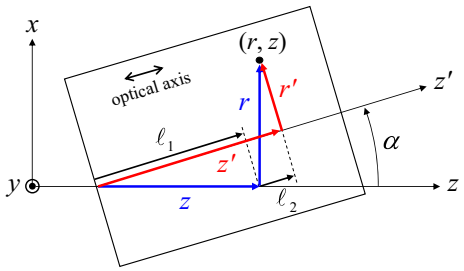

Fig. 7. Illustration of the titled geometry for the uniaxial crystal in the (x,z) plane.

$r'^2+z'^2=r^2+z^2$. We thus obtain

$$z' = z\cos\alpha + r\cos(\varphi-\psi)\sin\alpha, \tag{16}$$

$$r'^2 = r^2\left[1-\cos^2(\varphi-\psi)\sin^2\alpha\right] - rz\sin 2\alpha + z^2\sin^2\alpha. \tag{17}$$

With these new set of variables, the Eqs. (6) can be used to describe the oblique incidence case by using the transformation $G(r,z)\rightarrow G(r',z')$. In particular, for a given crystal length z, the choice of $\psi=\psi_0$ from Eq. (12) and $\alpha=\alpha_0$ from Eq. (15) allows to derive the expressions for the fields with the on-axis single charge vortex.

When the beam waist is large enough, it is possible to observe a well-defined on-axis single charge vortex at the output of the crystal, see Fig. 8. However, this requires a careful adjustment of the optical axis with respect to the beam propagation direction, $\alpha=\alpha_0$. Any departure from this critical incidence angle leads to an alteration of the resulting vortex, which eventually escapes from the beam for significant misalignment. Such an angular selectivity is experimentally illustrated in the upper part of Fig. 8 where $\lambda=632.8$ nm and $w=11$ μm. For example, if α_0 is chosen for a particular crystal length, $z=7$ mm in Fig. 8(a), the vortex is essentially distorted at other propagation lengths. On the other hand, for a fixed propagation length $z=6$ mm in Fig. 8(b), which corresponds to $\zeta\sim 10$, we see that an angular offset of few tenth of degree is enough to completely lose the vortex from the output beam. Furthermore, when comparing the experimental data to simulations we found that the coordinates of phase singularities in the quadrupole, derived in Eqs. (11), (12), and (15), do not exactly correspond to the optimal experimental parameters. In the numerical simulations which were performed using Eq. (1) we used $\psi_0^{\text{numerical}}=0.95\psi_0^{\text{approx}}$, where ψ_0^{approx} is given by Eq. (12), in agreement with the asymptotic mismatch between numerical and approximate solutions, $\left(\psi_0^{\text{numerical}}/\psi_0^{\text{approx}}\right)_{\zeta\gg 1}\simeq 0.96$, (see Sec. 3.2 and Fig. 5(f)). Moreover, we had to use $\alpha_0^{\text{numerical}}=0.865\alpha_0^{\text{approx}}$, where α_0^{approx} is given by Eq. (15), and we found a systematic experimental deviation from the optimal polar angle for the vortex direction, namely $\alpha_0^{\text{experiment}}-\alpha_0^{\text{numerical}}\simeq 0.1^\circ$. The latter discrepancy is therefore likely due to a residual experimental inaccuracy rather than asymptotic mismatch between numerical and approximate solutions since $\left(\alpha_0^{\text{numerical}}/\alpha_0^{\text{approx}}\right)_{\zeta\gg 1}\simeq 1.04$ (see Sec. 3.2).

4.2. Efficiency of polarization conversion

The polarization conversion dynamics in the tilted geometry (with $\alpha=\alpha_0$ and $\psi=\psi_0$) has an interesting and unexpected behavior. This is illustrated in Fig. 9 where the results obtained for the white light source are presented. Comparison between the rainbow-colored intensity profiles in Fig. 9(a) with the numerically obtained contour lines in Fig. 9(b) shows good qualitative agreement. Since the input angles α_0 and ψ_0 where chosen optimal for specific spectral

#116015 - $15.00 USD Received 20 Aug 2009; revised 18 Sep 2009; accepted 19 Sep 2009; published 24 Sep 2009
(C) 2009 OSA

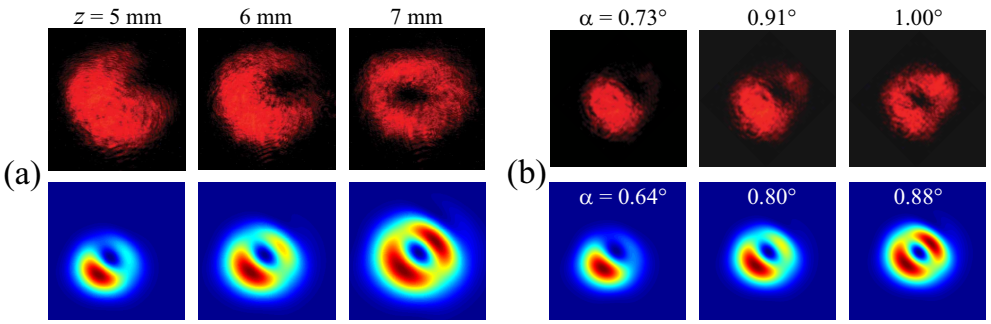

Fig. 8. Experimental (top row) and numerical (bottom row) results for generation of single-charge vortex beam, $\lambda = 632.8$ nm and $w = 11\ \mu$m. Output intensity patterns $I_{\|}$ for (a) three propagation lengths z for an internal angle $\alpha = 0.81^{\circ}$, and (b) different internal angles α with crystal length $z = 6$ mm. The experimental angles in (b, top) also take into account the refraction at the input interface of the crystal. Numerical results in panels (a,b) are false colored.

component (red with $\lambda = 630$ nm), other components propagate slightly offset, so that the vortex positions are noticeably shifted with respect to each other, e.g. see Fig. 6(c), which is mainly due to the $\sqrt{\lambda}$ dependence of α_0, see Eq. 15, rather than the dispersion of the birefringence $n_o(\lambda)$ and $n_e(\lambda)$ in the expression for α_0. Indeed we estimate $\Delta\sqrt{\lambda}/\sqrt{\lambda} \sim 28\%$ whereas $\Delta(n_o - n_e)^{-1}/(n_o - n_e)^{-1} \sim 9\%$ over the visible range 400–700 nm.

The powers in three main spectral component are measured for different crystal lengths, see Fig. 9(c). In that case, for each crystal length z, the angles α_0 and ψ_0 were adjusted to obtain a on-axis single charge vortex beam with the best possible quality. The relative powers are defined by the input spectrum, however, the behavior of any the quasi-monochromatic wavelength, or total power of the white-light beam, is normalized to the corresponding input power, the differences between spectral components is almost identical, as shown in Fig. 9(d). Note that the asymptotic behavior $P_{\perp}/P_{\|} \to 1/3$ is clearly observed for large propagation lengths, similar to the case of topological quadrupole in Figs. 3 and 4. However, the first stage of the propagation dynamics shown in Figs. 9(c, d) is drastically different from the case of normal incidence. It seems that $P_{\|} \to 0$ for $z \to 0$ which obviously contradicts our initial condition $P_{\|}(z = 0) = P_0$.

To answer this controversy we numerically integrate Eq. (1) for the parameters used in experiment, the results are shown in Figs. 9(e, f). For the red spectral component we calculate the z-evolution of powers for the set of crystal lengths $L = (1, ..., 10)$ mm with 1 mm step with the input parameters $\alpha_0(L)$ and $\psi_0(L)$. The corresponding propagation dynamics are shown in Fig. 9(e, black lines) where the values at $z = L$ are indicated with black circles. It is seen that the power $P_{\|}$ first rapidly decays from its initial value P_0, even below the level $P_0/2$ for the small crystal lengths, in sharp contrast with monotonous power decay for quadrupole in Fig. 3. With increase of L the power $P_{\|}$ progressively reaches the asymptotic value $3P_0/4$. As a result, the envelope of this process, the red curve in Fig. 9(e), approaches the asymptote from below, $P_{\|} < 3P_0/4$, as observed experimentally, see Fig. 9(d). The differences between three main spectral components are small, as shown in Fig. 9(f), that is also in good agreement with the experimental data in Fig. 9(d).

Interestingly, one could conclude from the asymptotic behavior that the tilted geometry is able to generate an optical vortex with 75% efficiency [see Fig. 9(b)], which is better than the 50% efficiency obtained from spin-orbit coupling in the normal incidence case with circularly polarized input beam. However, recalling that the present situation lead to a charge one vortex (associated with $\pm\hbar$ orbital momentum per photon) and that the circular case involves a

#116015 - $15.00 USD Received 20 Aug 2009; revised 18 Sep 2009; accepted 19 Sep 2009; published 24 Sep 2009
(C) 2009 OSA

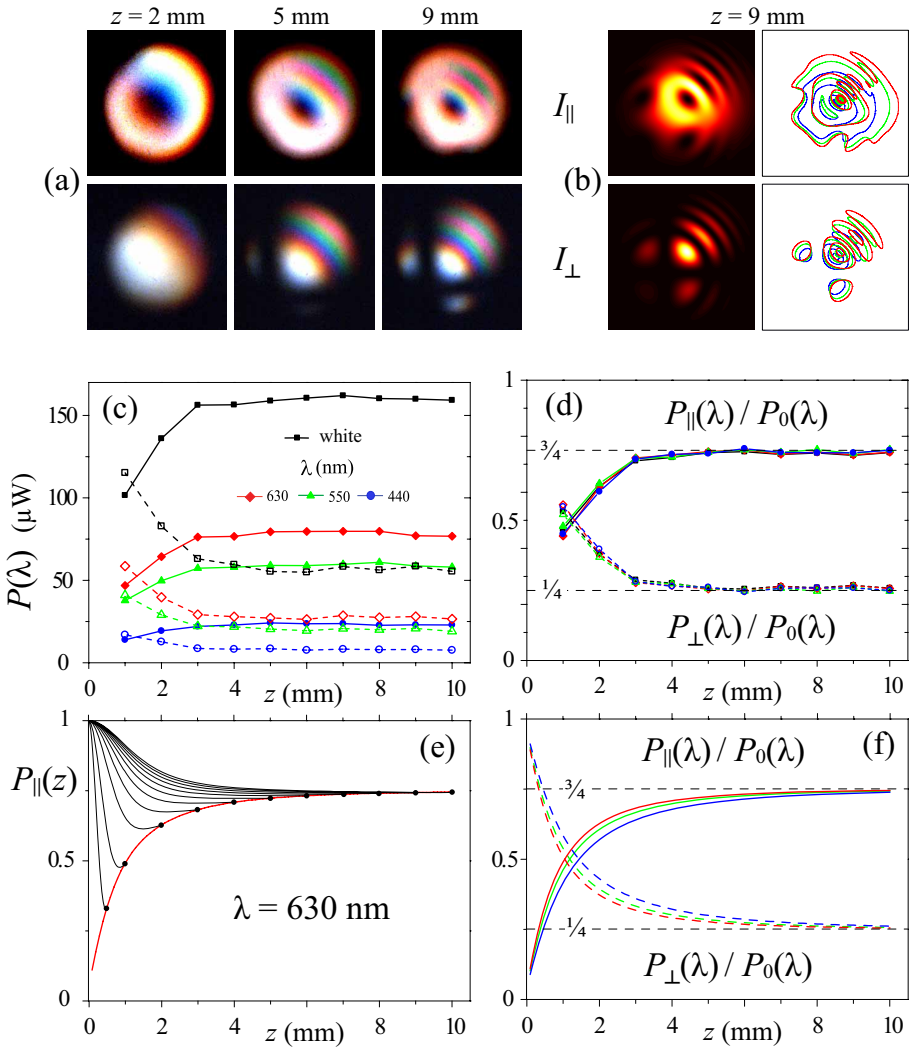

Fig. 9. Output intensity profiles $I_{\|}$ (upper line) and $I_{\perp}$ (bottom line) for (a) experimental data and (b) patterns calculated using Eq. (1). Note the relative shift of spectral components visible in the contour plots in panels (b), which explains the rainbow coloring of intensities in panels (a). Experimental spectrally resolved power measurements in (c) and (d), where solid (dashed) curves refer to $P_{\|}$ ($P_{\perp}$), are compared with numerical results in (e) and (f) for an input Gaussian beam with $w = 6\,\mu$m. In panels (c,d,f) the color labeling is red, green and blue for $\lambda = 630$, 550 and 440 nm, respectively.

#116015 - $15.00 USD Received 20 Aug 2009; revised 18 Sep 2009; accepted 19 Sep 2009; published 24 Sep 2009
(C) 2009 OSA

charge two vortex (respectively associated with $\pm 2\hbar$ momentum), the overall net generation of orbital angular momentum per photon is more favorable in the circular polarization interaction geometry. Moreover, we notice that for large crystal thicknesses, the output beam in the tilted case eventually leads to an off-axis multipole structure, whose total orbital angular momentum results from the non trivial superposition of single charge phase singularities having alternating signs and that is beyond the scope of the present work.

5. Conclusions

We derive and analyze the solution of the paraxial wave equation in uniaxial crystals for two distinct cases: the generation of topological quadrupole at the normal incidence of linearly polarized Gaussian beam and the generation of a single charge on-axis optical vortex at oblique incidence. We have theoretically and experimentally investigated the dynamics and efficiency of polarization conversion inside a uniaxial crystal. In both cases the efficiency of the polarization conversion reaches 25% for long crystals, i.e. the efficiency of the generation of optical vortices approaches 75%. However, at small crystal lengths there are significant differences, in particular the efficiency of single vortex generation can be below 50%. We derive the optimal parameters for single vortex generation in the case of oblique incidence with taking into account physical features of uniaxial crystal, including chromatic dispersion of the crystal and the parameters of an input beam power. We expand the results to the case of white-light beams. In particular, we show the angle variation defining the individual optical vortices trajectories in multipole as a function of the propagation distance for three different spectral components. We found that this angle decreases with the propagation distance inside the crystal and increases with the wavelength. Our results will serve as a practical guide in using uniaxial crystal for generation of singular beams for various applications.

This work was supported by the Australian Research Council.

#116015 - $15.00 USD Received 20 Aug 2009; revised 18 Sep 2009; accepted 19 Sep 2009; published 24 Sep 2009
(C) 2009 OSA